Contents lists available at ScienceDirect

Thermal Science and Engineering Progress

journal homepage: http://ees.elsevier.com

Journal Cover Image

Nox emission reduction reaction of ammonia-hydrogen with self-sustained pulsating oscillations

Siliang Ni [a], Dan Zhao [a,*], W.W. Wu [b], Yiheng Guan [b]

[a] Department of Mechanical Engineering, University of Canterbury, Private Bag 4800, Christchurch 8041, New Zealand
[b] School of Energy and Power Engineering, Jiangsu University of Science and Technology, Zhenjiang 212003, China

ARTICLE INFO

Keywords
NOx emission
Hydrogen
Pulsating oscillations
Ammonia

ABSTRACT

Unlike hydrocarbon fuel, ammonia (NH_3) is an alternative but promising carbon-free renewable fuel. The utilization of NH_3 as energy resource can effectively reduce greenhouse gas CO_2 emission. Here we explore interdisciplinary physics of ammonia-hydrogen-fueled combustion-sustained pulsating oscillations and its impact on NOx emission via numerical simulations. A longitudinal combustor with both ends acoustically open is developed. The premixed flame and constant-temperature heat exchangers are implemented upstream and downstream. With the model validated, it is applied to gain insights on the effects of 1) the mass flow rate $\dot{m}$ of the fuel mixture, 2) the hydrogen mass fraction w_{H2} relative to the fuel mixture, and 3) the temperature T_H of the heat exchangers. It is found that nonlinear pulsating oscillations could be generated, depending on $\dot{m}$ Furthermore, the oscillation amplitude and frequency are shown to strongly depend on $\dot{m}$ andw_{H2}. In addition, as w_{H2} is reduced from 45% to 15%, intermittent oscillations with a period of 10^0 s are observed to superimpose on the acoustic resonance nature of the combustor with a time scale of 10^{-2} s. Finally, varying temperatures of the heat exchanger are found to affect NOx generation and decrease the amplitude of the pulsating oscillations somehow.

1. Introduction

As a clean fuel of high efficiency, hydrogen is widely utilized in combustion devices for energy supply [1]. However, there is a potential to bring about explosion hazard due to its strong volatility and high reactivity during storage and transport [2,3]. Besides hydrogen, ammonia is one of the carbon-free options [4] to supply the power to the globe [5] via gas turbines [6], internal combustion engines [7,8] and fuel-cells. Compared with hydrogen, ammonia is more attractive because of its low production cost and high volumetric energy density, which is easier to distribute and process under the existing infrastructure [9]. Burning ammonia does not necessarily increase NOx emissions from engines [10]. Reiter and Kong [8,10] experimentally showed that when ammonia-burnt energy release did not exceed 60% of the mixture of ammonia-methane, lower NOx emissions were obtained. In addition, applying biodiesel-ammonia produces similar combustion and emission performance by using diesel fuel-ammonia.

Although ammonia is a promising sustainable fuel, it has some unattractive features, such as a lower flame speed, lower heat of combustion [11], higher heat of vaporization and narrower flammability limits in comparison with conventional hydrocarbon fuel [12]. To remedy this, it has been proposed to use carbon-free ammonia (NH_3) instead of hydrocarbons as an additive in H_2 flames [13,14], while reducing the problem of global warming caused by carbon dioxide emissions. In order to study the combustion performance of NH_3 as an additive in premix and non-premix H_2/air flames, Joo and Lee et al. [15,16] conducted a series of experimental and numerical investigations. It was found that the combustion stability limit decreases obviously with the increase of NH_3 ratio. Valera et al. [17] analyzed the flame characteristics and chemical reaction data of NH_3/H_2/air swirling combustion under rich conditions through experiments and numerical simulations. Results show that the mixture of 70% NH_3 and 30% H_2 can be used as fuel for stable combustion in gas turbine. In addition, the increase of inlet gas temperature is beneficial for the improvement of combustion efficiency. Lhuillier et al. [18] conducted experimental research on the performance and combustion characteristics of a spark ignition engine powered by NH_3/H_2/air mixture. The results show that when the proportion of hydrogen in the mixture is over 20%, the thermal recirculation and combustion stability can be improved. Moreover, the output power can be compared with that of conventional fuels.

* Corresponding author.
E-mail address: dan.zhao@canterbury.ac.nz (D. Zhao)

https://doi.org/10.1016/j.tsep.2020.100615
Received 21 April 2020; Received in revised form 15 June 2020; Accepted 23 June 2020
Available online xxx
2451-9049/© 2020.

UNCORRECTED PROOF

Burning ammonia does not emit carbon dioxide. However, it will produce nitrogen oxides, which have direct or indirect effects on human health. Therefore, how to reduce nitrogen oxide emissions when using ammonia gas as fuel is another problem that needs to be investigated. For better understanding the mechanism of NOx formation, Duynslaegher et al. [19,20] carried out dynamic simulation of ammonia combustion at low pressure. Reduced mechanism containing of 19 chemical species and 80 elementary reactions was obtained by comparing flame structure. It was found that when the fuel–air ratio was higher than 1, the influence of pressure and temperature on NO can be neglected. Li et al. [14,21] experimentally evaluated NOx formation and combustion characteristics of the mixture of H_2 and NH_3 at different fuel–air ratio and initial H_2 concentration in the mixture. It was found that NH_3 burning velocity is increased with increased H_2 concentration. Furthermore, thermal NOx production is found to be lower than pure H_2/air combustion. Furthermore, the exothermic rate of NH_3 flame is proportional to the strength of OH and N radical formation. In order to predict the flame speed and ignition delay time of ammonia gas during combustion, Otomo et al. [22] proposed a new combustion mechanism which well fitted the experimental data of laminar flame at different equivalent ratios and provided an appropriate condition for reducing NO emissions. Hussein et al. [23] investigated the emission of nitrogen oxides by injecting different amounts of ammonia and hydrogen mixtures into a swirl burner under preheating conditions for combustion. Results show that when the ratio of ammonia-hydrogen is 60–40%, the conversion rate of ammonia is the highest with high NO emission.

Ammonia combustion produces heat release to supply power output from the engine. Such heat release process is typically unsteady [24,25]. On the other hand, the gas turbine combustor is acoustically resonant [26]. When the unsteady heat release is coincidently aligned with the acoustic resonant nature, self-sustained pulsating oscillations also known as thermoacoustic instability [27,28] will occur. It is characterized with large-amplitude limit cycle oscillation. Such limit cycle is a closed trajectory in phase space having the property that at least one other trajectory spirals into it either as time approaches infinity or as time approaches negative infinity [29,30]. It could enhance or deteriorate the NO formation in the ammonia combustion. Although there are many studies on reducing NOx emission in ammonia combustion, there is a lack of experimental and numerical investigations on how NOx is generated in the presence of limit cycle oscillations in a combustor. In addition, whether a secondary heat source or a heat exchanger in the combustor will affect NOx emission is not reported in the literature, to the best knowledge of the present authors. Lack of these studies partially motivated the present work.

In this work, numerical studies are conducted on an acoustically open-open combustor with the blend of NH_3-H_2 fueled. The turbulence model k-epsilon and multiple-steps NH_3/H_2 blended combustion (EDC model) are used. The numerical model, governing equations and mesh independent study are described in Sect. 2. In Sect. 3, the effects of 1) the total mass flow rate of the $NH_3/H_2/O_2$ mixture, and 2) the H_2 mass fraction w_{H2} of the mixture of $NH_3/H_2/O_2$ are evaluated and discussed. In Sect. 4, besides the upstream flame, a secondary heat source consisting of 3 constant-temperature heat exchangers is implemented on the downstream half of the combustor. The effect of varying heating temperature of the heat exchangers are examined and discussed. Key findings are summarized in Sect. 5.

2. Modelled premixed combustor with NH_3-H_2 fueled

2.1. Model set-up and governing equations

The open – open combustor is shown schematically in Fig. 1. As the hydrogen-ammonia and oxygen mixture is injected to the tube, air is squeezed continuously from bottom inlet of the combustor with a

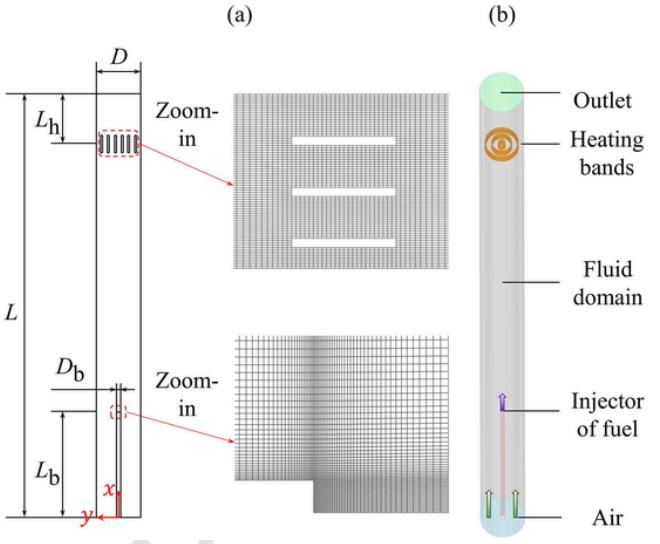

Fig. 1. (a) 2D schematic with structure dimensions of key parameters and local mesh diagrams near fuel inlet and heat exchangers, (b) the corresponding 3D model of the acoustically open-open combustor with a fuel injector and heat exchangers of constant temperature confined on the upstream and downstream half. The overall length L of the modelled combustor is set to 1000 mm. The axial length of the fuel injector L_b is 250 mm while the distance between the heat exchangers of outlet L_h is 125 mm. The combustor inner diameter is set to 50 mm and the inner diameter of the injector D_b is 5 mm.

constant pressure difference. Three heat exchangers with an axial length of 15 mm are placed 125 mm away from the top combustor open end. The heat exchangers with constant temperature are implemented as a 'noise damper/amplifier' [31,32] to minimize/maximize the combustion-driven pulsating oscillations. However, the number of heat exchangers and its surface area can be varied. For demonstration, we choose 3 heat exchangers. The fuel injector is placed at 250 mm away from the bottom open end. Structural meshes are generated by Hypermesh 14.0. To improve the simulation accuracy, refined mesh is utilized at the regions near the fuel injector and heat exchangers.

The dynamic chemical reaction-flow-acoustics interactions in the modelled combustor can be simulated by using a series of governing equations such as fluid dynamics and chemical reactions [33,34]. These equations are coupled and need to be solved simultaneously [35]. Besides the thermodynamics state equation, the other governing equations are given as follow

1) Mass conservation:

$$\frac{\partial \rho}{\partial t} + \frac{\partial (\rho u_i)}{\partial x_i} = 0 \tag{1}$$

where ρ denotes density, u denotes fluid velocity, t denotes time and x is the spatial dimension.

2) Momentum conservation:

$$\frac{\partial (\rho u_i)}{\partial t} + \frac{\partial (\rho u_i u_j)}{\partial x_i} = -\frac{\partial p}{\partial t} + \frac{\partial}{\partial x_i}\left[\mu_t \left(\frac{\partial u_i}{\partial x_j} + \frac{\partial u_j}{\partial x_i}\right) - \frac{2}{3}\mu_t \frac{\partial u_k}{\partial x_k}\right]\delta_{ij} + \rho g \delta_{ij} \tag{2}$$

where p denotes pressure, μ_t denotes turbulent viscosity, and δ_{ij} is Kronecker delta function, and $\delta_{ij} = 1$, when $i = j$; otherwise $\delta_{ij} = 0$.

3) Species conservation:

$$\frac{\partial (\rho w_k)}{\partial t} + \frac{\partial (\rho u_i w_k)}{\partial x_i} = \frac{\partial J_k}{\partial t} + R_k \tag{3}$$

where w_k is the mass fraction of k^{th} species, J_k denotes the diffusion of

UNCORRECTED

the species, and R_k denotes the production of the species due to chemical reaction.

4) Energy conservation:

$$\frac{\partial(\rho E)}{\partial t}+\frac{\partial\left[u_i(\rho E+p)\right]}{\partial x_i}=\frac{\partial y}{\partial x_j}\left(k_{\text{eff}}\frac{\partial T}{\partial x_j}-\sum_j h_j J_j+u_i\left[\mu_{\text{eff}}\left(\frac{\partial u_i}{\partial x_j}+\frac{\partial u_j}{\partial x_i}\right)-\frac{2}{3}\mu_{\text{eff}}\frac{\partial u_k}{\partial x_k}\right]\delta_{ij}\right) \tag{4}$$

where E is the total energy, k_{eff} denotes the effective thermal conductivity, h is enthalpy, μ_{eff} denotes effective viscosity, and T is the temperature.

To capture turbulence impact on the fluid flow and flame based on Boussinesq hypothesis, the turbulent viscosity μ_t is introduced and calculated under RNG $k-\varepsilon$ model in ANSYS FLUENT 19.2. The turbulent viscosity μ_t can be expressed as:

$$\mu_t=0.0845\rho\frac{k^2}{\varepsilon} \tag{5}$$

where k denotes the turbulent kinetic energy and ε denotes the turbulent dissipation. The turbulent kinetic energy k and dissipation ε can be determined using transport equations:

$$\frac{\partial(\rho\varepsilon)}{\partial t}+\frac{\partial\left(\rho k u_i\right)}{\partial x_i}=\frac{\partial}{\partial x_j}\left(\alpha_k\mu_{\text{eff}}\frac{\partial k}{\partial x_j}\right)+G_k+G_b-\rho\varepsilon-Y_M \tag{6}$$

and

$$\frac{\partial(\rho\varepsilon)}{\partial t}+\frac{\partial\left(\rho\varepsilon u_i\right)}{\partial x_i}=\frac{\partial}{\partial x_j}\left(\alpha_\varepsilon\mu_{\text{eff}}\frac{\partial\varepsilon}{\partial x_j}\right)+C_{1\varepsilon}\frac{\varepsilon}{k}\left(G_k+C_{3\varepsilon}G_b\right)-C_{2\varepsilon}\rho\frac{\varepsilon^2}{k}-R_\varepsilon \tag{7}$$

where G_k represents the generation of turbulence kinetic energy due to the mean velocity gradients, G_b denotes the generation of turbulence kinetic energy due to buoyancy, Y_M is the contribution of the fluctuating dilatation in compressible turbulence to the overall dissipation rate, α_k and α_ε are the inverse effective Prandtl numbers for k and ε respectively while $C_{1\varepsilon}$ to $C_{3\varepsilon}$ are modelling constants.

Here eddy-dissipation model is chosen for calculating the production term R_k, it is given as :

$$R_k=min\left(4\nu_k' MW_k\rho\frac{\varepsilon}{k}\min_i\left(\frac{w_i}{\nu_i' M_i}\right),2\nu_k' MW_k\rho\frac{\varepsilon}{k}\frac{\sum_i w_i}{\sum_j^N\nu_j'' MW_j}\right) \tag{8}$$

where MW_k denotes the molecular weight of k^{th} species, ν_k' represents the stoichiometric coefficient for the k^{th} species (i.e. chemical reactant). ν_j'' denotes the stoichiometric coefficient for the j^{th} species in the combustion products.

In order to investigate the variation of reactant and combustion product species, the mole fraction χ_k is defined as:

$$\chi_k=\frac{n_k}{n_{tot}} \tag{9}$$

where n_k denotes the molecular weight of k^{th} species and n_{tot} denotes the total amount of molecular weight of all species. Detail flow conditions are summarized in Table 1.

Table 1
Condition settings of 5 cases.

Case number	Mass flow rate $\dot{m}$ (kg/s)	Mass fraction of hydrogen $^{W}H_2$
Case-1	1.0×10^{-6}	45%
Case-2	5.0×10^{-6}	45%
Case-3	1.0×10^{-5}	45%
Case-4	1.0×10^{-5}	15%
Case-5	1.0×10^{-5}	88.4%

2.2. Mesh-independence studies

In this work, the pressure-based solver is selected to solve the described governing equations above. The time step Δt is set to be $\Delta t=1.0\times10^{-4}s$ with a second-order discretization. In aspect of spatial discretization, except for the pressure and turbulence dissipation (second-order upwind), all the equations are solved with third-order MUSCL scheme. In order to keep ammonia burning at high concentrations and obtain sufficient heat release for forming self-excited oscillation, the mass fraction of oxygen in the fuel injector is fixed to 11.6%. The gravitational acceleration is set to −9.81 m/s^{2}which is opposite to the flow direction. In addition, the species transport model and eddy dissipation concept are chosen for modelling.

The boundary conditions can be summarised as: 1) all walls including combustor and fuel injector are set to be adiabatic; 2) prescribed constant temperature, i.e. T = 300 K for $0.0\le t\le t_h$ s, T starts to increase from 300 K to 1300 K at $t=t_h$ s and t_h denotes the actuation time of the heat exchangers; 3) the fuel injector is a mass flow inlet; 4) the bottom and top ends of the modelled combustor are set to be pressure inlet and outlet respectively with a constant pressure difference.

The meshed models are first simulated using a steady time solver. When a stable flame is obtained, it is changed to a transient time solver. A series of monitoring points are set to observe and record the self-sustained oscillations of each acoustic/flow parameter in time domain. The recorded data are then post-processed by MATLAB for graphing and further analysis.

Mesh-independence study is conducted first to confirm the mesh we choose is acceptable to investigate the NH_3/H_2-fueled pulsating combustion. Fig. 2 illustrates the calculated temperature and velocity contours, as 3 different number meshes are applied. No clear difference is observed. However, a closer observation is made on Fig. 3. It illustrates the time evolution of the pressure and velocity along the centreline of the combustor and middle-point. It can be seen that the medium mesh is applicable, since it produces as good results as that from fine mesh.

3. Results and model validation

As the mixture of NH_3/H_2 is burned, a cone-shaped flame is formed along the centreline of combustor. Fig. 4 illustrates the static temperature, as the inlet mass flow rate $\dot{m}$ and mass fraction of hydrogen $^{W}H_2$ are set to three different values. It can be seen that the flame length and high temperature region is dramatically increased with increased $\dot{m}$ and/or $^{W}H_2$. However, a detached flame is observed and stabilized in some axial distance downstream when $\dot{m}=1.0\times10^{-6}kg/s$ or $^{W}H_2=15\,\%$. The flame zone can be regarded as an area of intense reaction at the leading edge of premixed fuel and the tail flame which is formed by the remaining fuel reignited backwards. Comparing to ammonia, the density of hydrogen is much lower but the diffusion coefficient is larger. Therefore, the hydrogen has a high-flame propagation velocity. As the mass flow rate is too small or ammonia is dominant in the fuel mixture, the total heat release is deficient to ignite ammonia completely. After being transported to downstream, most of the fuel

UNCORRECTED PROOF

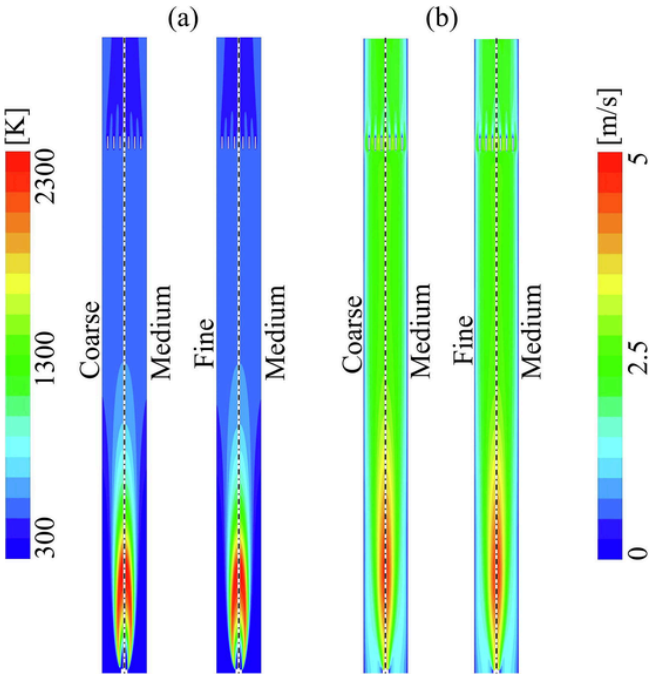

Fig. 2. Comparison of the predicted contours of the (a) temperature and (b) velocity, as coarse (12,934 elements), medium (25,868 elements) and fine (51,736 elements) meshes are applied when $w_{H_2} = 45\ \%$ and $\dot{m} = 1.0 \times 10^{-5} kg/s$.

mixture (NH_3 and H_2) is burnt near the leading edge, leaving large volumes of very fuel-lean gases to diffuse downstream. If the flame further moves away from the inlet, it will finally step into a region where no combustion is supported anymore due to low density of reactants and all chemical reactions cease abruptly [35]. Note that previous studies have confirmed that the detached flame in longitudinal combustors are quite often observed However, none of the currently-available theories for flame stabilization are satisfactory and further experimentations are needed for predicting the properties of flame blowout [36,37]. It is found that flame instability may play a role in leading to the onset of blowout process and the high strain rate encountered by the flame base in the onset region should be considered as a prominent factor for the blowout process [38,39]. With different viscous models tested, LES is found to be able to predict lean blow-out accurately in gas turbine combustors for different fuels [40].

3.1. Effect of the total mass flow rate $\dot{m}$

Unsteady heat release has been known as a monopole-like energy-efficient sound source to generate acoustic perturbations [41]. These acoustic disturbances can propagate through the combustion system and partially reflected back to the combustion/flame zone. This may strengthen the unsteady heat release. However, such acoustic fluctuations can decay or amplified into large-amplitude pulsating oscillations (also known as limit cycle). This needs to be further studied.

As the change of mass flow rate can dramatically affect the characteristics of flame, it is significant to evaluate the effect of the total mass flow rate $\dot{m}$on producing pulsating oscillations. Fig. 5 illustrates the time variation of the acoustic pressure recorded along the centerline of the tube at $x/L = 0.5$, as $w_{H_2} = 45\ \%$ and $\dot{m}$ is set to 3 different values. It can be seen from Fig. 5(a)-(c) that initial small-amplitude pressure fluctuations rapidly grow into limit cycle. Furthermore, the limit cycle amplitude depends strongly on $\dot{m}$. In addition, the time taken to form such limit cycle is observed to be decreased with increased $\dot{m}$. The corresponding phase diagram (see Fig. 5(d)) of a circle reveals that limit cycle oscillations are associated with only one dominant frequency.

To gain insights on the acoustic signature of such combustion-driven pulsating oscillations, the mode shapes of the acoustic pressure fluctuations along the axial direction are numerically determined and compared with the theoretical modelling of standing wave in an open-open thermoacoustic combustor [42]. This is shown in Fig. 6(a). Periodic variation of the calculated mode-shape from the present model is shown in Fig. 6(b). It can be seen that the maximum pressure amplitude occurs near the center-point of the combustor along the axial direction. Both inlet and outlet are corresponding to a pressure node (i.e. $|p(t)| \approx 0$). This confirms that longitudinal standing-wave is present when combustion-excited limit cycle occurs.

To validate the numerical model and to gain further insights, experimental studies are conducted on an acoustically open-open combustor with a total axial length of 1 m and propane fueled. Detailed experimental setup information can be found in literature [42]. Fig. 6(c) shows the comparison of the experimentally measured pressure spectrum [43] with the numerically modeled one. Although slight discrepancies can be observed, the dominant frequency and amplitude agrees well with the numerical results. The discrepancies in terms of the dominant mode frequency and amplitudes depend on the mass flow rate of the fuel mixture, which determines the total heat release and the mean temperature of the combustor.

As NH_3/H_2 mixture is burned, the instantaneous temperature at $x/L = 0.5$ is recorded in real time and illustrated in Fig. 7 (a)-(c) corresponding to 3 different $\dot{m}$. It shows that self-excited oscillations can

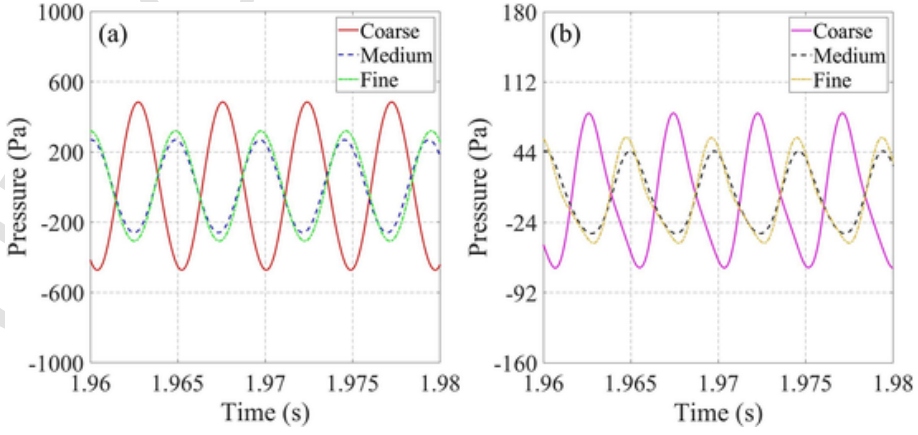

Fig. 3. Mesh independent studies of calculated acoustic pressure at (a) the middle point of central axis and (b) the end of central axis when $w_{H_2} = 45\ \%$ and $\dot{m} = 1.0 \times 10^{-5} kg/s$.

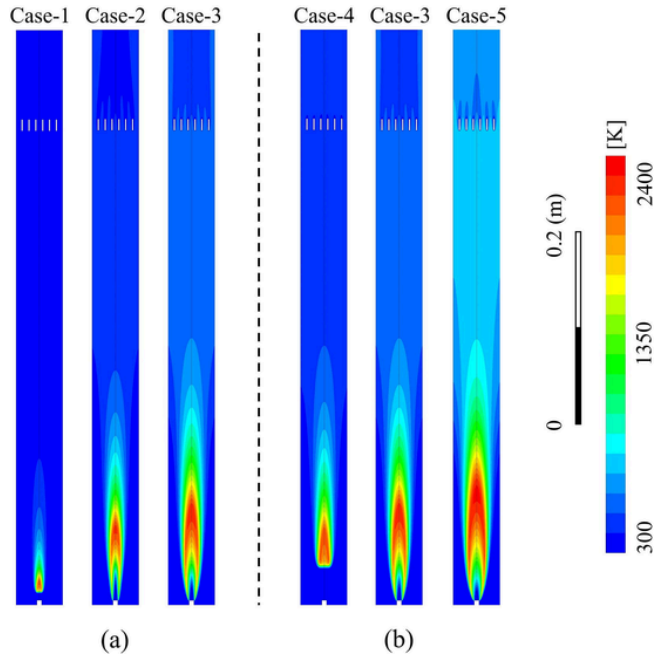

Fig. 4. Calculated temperature of NH_3/H_2-fuelled flame when (a) $^{W_{H_2}}$ is the same with different $\dot{m}$ and (b) $\dot{m}$ is the same with different. $^{W_{H_2}}$

lead to temperature fluctuations and so the entropy is increased. Furthermore, the temperature oscillations are quasi-periodic. It is clear from Fig. 7(d) that the temperature gradient " dT/dt" is floating up and down. Moreover, the temperature fluctuation amplitude is significantly decreased with decreased$\dot{m}$.

The acoustic velocity variation in time domain and its corresponding spectrum in frequency domain with $\dot{m}$ set to 3 different values are shown in Fig. 8(a) and (b) respectively. It can be seen from Fig. 8(a) that as the mass flow rate is increased, the velocity fluctuating amplitude is increased, besides the mean velocity is increased dramatically. The frequency spectrum shown in Fig. 8(b) reveals that as $\dot{m}$ is increased from 1.0×10^{-6} kg/s(blue dash curve) to $1.0 \times 10^{-5} kg/s$ (green solid curve), mode-switching occurs, i.e. the dominant mode is found to switch from higher frequency (approximately 380 Hz) to lower one (about 180 Hz). Furthermore, the dominant peak amplitude is dramatically increased. Fig. 8(c) shows the phase diagram of the acoustic velocity fluctuation as $^{W_{H_2}} = 45\backslash\ \%$ and $\dot{m} = 5.0 \times 10^{-6} kg/s$, (corresponding to red dash dot curve in the velocity spectrum in Fig. 8(b)). Non-circle shape in Fig. 8(c) indicates that there are at least two dominant modes with comparable amplitudes. It means that nonlinearity is intensified with increased mass flow rate and increased heat release rates, as shown in Fig. 9(a). The corresponding phase diagrams of the instantaneous heat release rates are shown in Fig. 9(b)-(d). Since the mean flow in the present modeled combustor is small [44], the heat release is identified to be the dominant source of nonlinearity, as illustrated in the wavy-shaped circle phase diagrams. This is consistent with the previous findings in Ref. [45-47].

As a renewable fuel, ammonia has relatively lower mass diffusivity and higher ignition temperature than hydrogen. Ammonia combustion will produce undesirable NO and NO_2, which is a serious environmental concern. Thus it would be interesting to evaluate the chemical reactions of NH_3 and H_2 and the combustion products, before and after actuating the heat exchangers in the combustor. Fig. 10 shows the chemical reactants and combustion products variation in radial (i.e. r/R) and axial (i.e. x/L) directions, as $\dot{m}$ is set to two different values. The purple colored solid curves (see Fig. 10(a, c, e and g)) represent the molar distribution of NH_3 in radial (i.e. r/R) and axial (i.e. x/L) directions.

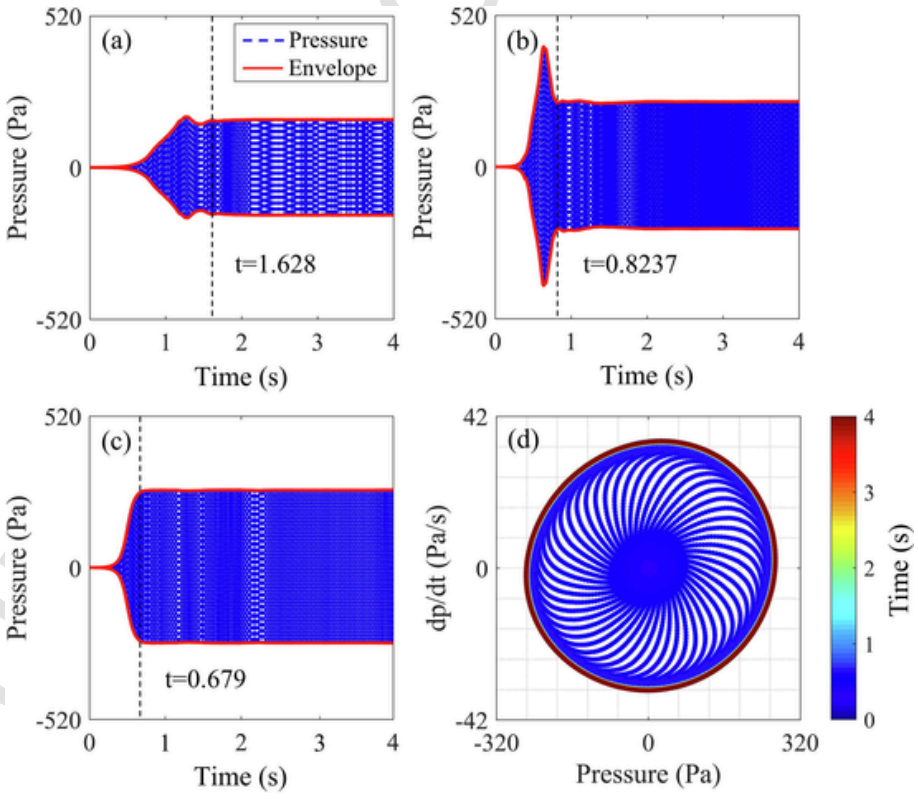

Fig. 5. Variation of the acoustic pressure in time domain, as $^{W_{H_2}} = 45\backslash\ \%$, and $\dot{m}$ is set to (a)$\dot{m} = 1.0 \times 10^{-5} kg/s$; (b) $\dot{m} = 1.0 \times 10^{-5} kg/s$, (c) $\dot{m} = 1.0 \times 10^{-5} kg/s$; (d) the corresponding phase diagram, as $^{W_{H_2}} = 45\backslash\ \%$and $\dot{m} = 1.0 \times 10^{-5} kg/s$.The time at which the limit cycle is reached is shown with dash line.

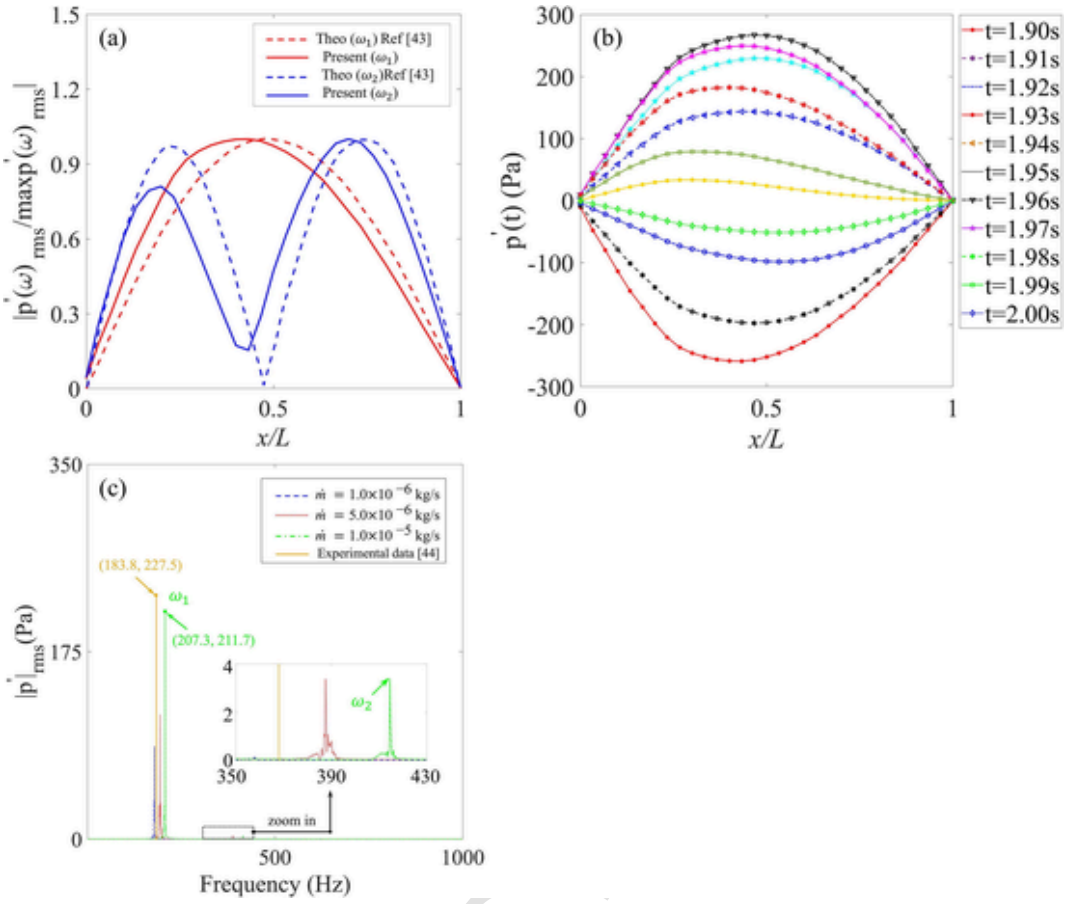

Fig. 6. (a) Comparison of the calculated mode-shapes of the acoustic pressure fluctuations in axial direction with the theoretical one [42], (b) periodic variation of the longitudinal mode-shape, (c) comparison the acoustic pressure spectrum with the experimental data [43] of an open-open combustor, as $\dot{m} = 1.0 \times 10^{-5} kg/s$, and the mass fraction of H_2 is set to be $w_{H_2} = 45\backslash\,\%$.

Fig. 10(a, b, e and f) shows the mole fraction of both hydrogen and ammonia drops sharply in axial direction. 100% burning of H_2 is achieved after the reaction zone ($x/L \geq 45\%$). Comparing Fig. 10(a) and (e) reveals that the molar fraction of H_2 and NH_3 continuously and gradually drop as $\dot{m} = 1.0 \times 10^{-6} kg/s$, while it remains stable in preheating region as $\dot{m} = 1.0 \times 10^{-5} kg/s$. The profile of O_2 is increased first and then decreased in axial direction, when ṁ is set to $\dot{m} = 1.0 \times 10^{-6} kg/s$ A maximum value is observed at about $x/L = 0.18$. This is consistent with the detached flame as shown in Fig. 4(a). As far as NO and NO_2 emissions are concerned, the molar fraction of NO, as the indicator of incomplete reaction of ammonia, is increased and then decreased, and finally 'saturated', no matter what ṁ is set to (see Fig. 10 (b) and (f)). However, the molar fraction of NO and NO_2 at the combustion outlet ($x/L = 1.0$) is found to increase with increased ṁ. In terms of radial profiles (see Fig. 10(c, d, g and h)), similar consequences can be concluded. The unburned fuel of both H_2 and NH_3 is increased with the decrease of ṁ (see Fig. 10(c) and (g)). Moreover, the conversion rate of NO_2 is also increased when ṁ decreases. It can be seen that the mole fraction of NO is almost 4 times larger than that of NO_2 as $\dot{m} = 1.0 \times 10^{-5} kg/s$ However, the distribution is absolutely contrary as ṁ decreases to1.0×10^{-6}kg/s.

3.2. Effect of hydrogen mass fraction w_{H2}

The effect of blending hydrogen with ammonia on generating combustion-driven pulsating oscillations are shown in Fig. 11. It is apparent that limit cycle can be generated, no matter what mass fraction w_{H2} of H_2 is set. However, intermittent oscillations at a frequency of approximately 0.8 Hz occur, as wH_2 is se to 15% and the maximum amplitude can be as large as 800 Pa. By comparing Fig. 11(b) with Fig. 11(c), it can be seen that the amplitudes are almost the same which indicates that the mass fraction of H_2 has a little influence when $w_{H2} \geq 45\%$. When $w_{H2} = 15\%$, the zig-zag circle-shape phase diagram shown in Fig. 11(d) indicates stronger nonlinearity. Such large-amplitude intermittency oscillations are unwanted in propulsion systems, since it may lead to fracture of the brittle material or may cause deformation of the ductile material [48,49]. In general, this study confirms the strong impact of hydrogen on producing and the characteristics of the NH_3-H_2-combustion-driven pulsating oscillations.

4. Heat exchangers impact on limit cycle and NOx emission

Implementing the heat exchanger with constant temperature at downstream is to study its impact on amplifying or damping pulsating combustion-driven oscillations. Fig. 12(a) shows the performance of the heat exchangers actuated at t = 2.0 s by increasing its surface temperature from 300 K to 1300 K in terms of acoustical potential energy $E_a(t)$.$E_a(t)$ is defined as:

$$E_a(t) = \frac{\frac{\omega}{2\pi}\int_t^{t+2\pi/\omega}\left[p'_{(t)}\right]^2 dt}{2\gamma p_0} \tag{18}$$

where $p'_{(t)}$ denotes the acoustic perturbation, ω represent the radian frequency, while γ is set to 1.4 constantly and $p_0 = 1.01325 \times 10^5$ pa denotes atmospheric pressure. It can be seen that the potential energy *E*(a) of the combustion-driven limit cycle is attenuated somehow de-

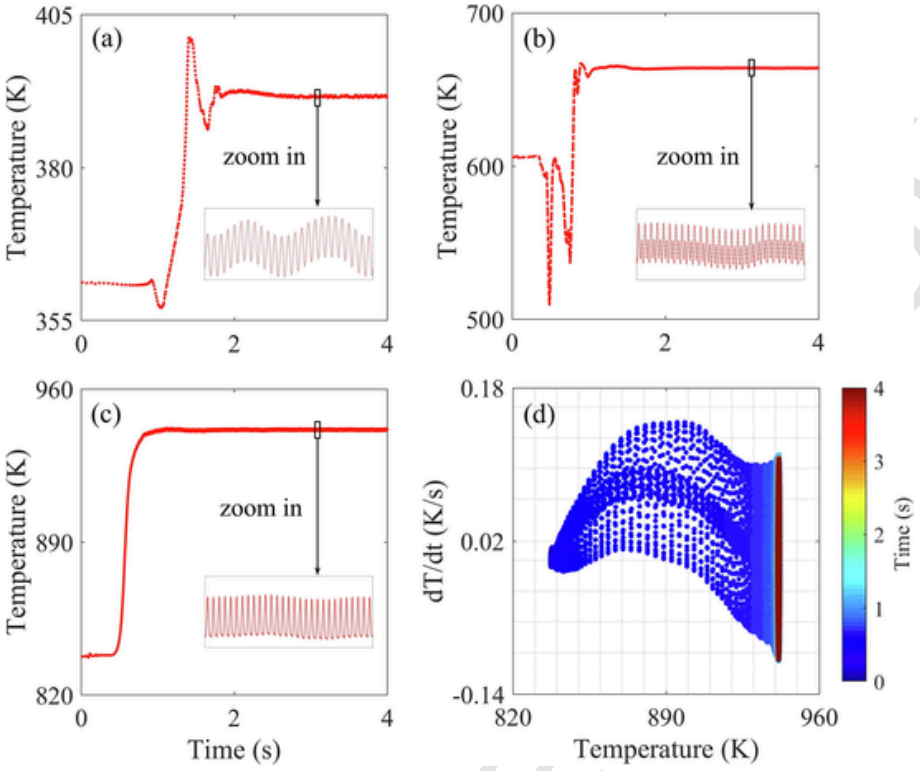

Fig. 7. Temperature variation in time domain, as w_{H_2}= 45\ %, and ṁ is set to (a) $\dot{m} = 5.0 \times 10^{-6} kg/s$, (b) $\dot{m} = 5.0 \times 10^{-6} kg/s$, (c) $\dot{m} = 1.0 \times 10^{-5} kg/s$; (d) the corresponding phase diagram, as w_{H_2}= 45\ % and $\dot{m} = 1.0 \times 10^{-5} kg/s$.

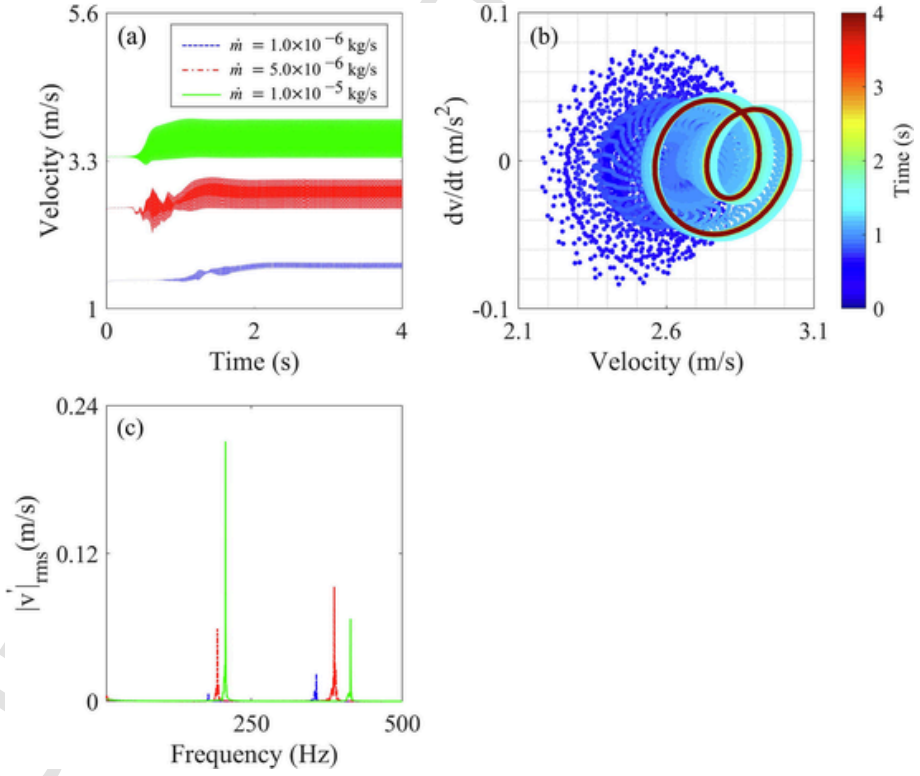

Fig. 8. (a) Time variation of the acoustic velocity at x/L = 0.5, (b) acoustic velocity spectrum in frequency domain, and (c) the corresponding phase diagram ($\dot{m} = 5.0 \times 10^{-6} kg/s$ and w_{H_2}= 45\ %).

pending on the mass flow rate and the temperature of the heat exchanger. As $\dot{m} = 1.0 \times 10^{-5} kg/s$, the acoustical potential energy E_a is reduced by 22.3% from t = 2.0 s to t = 4.0 s. Fig. 12(b) shows the cor-

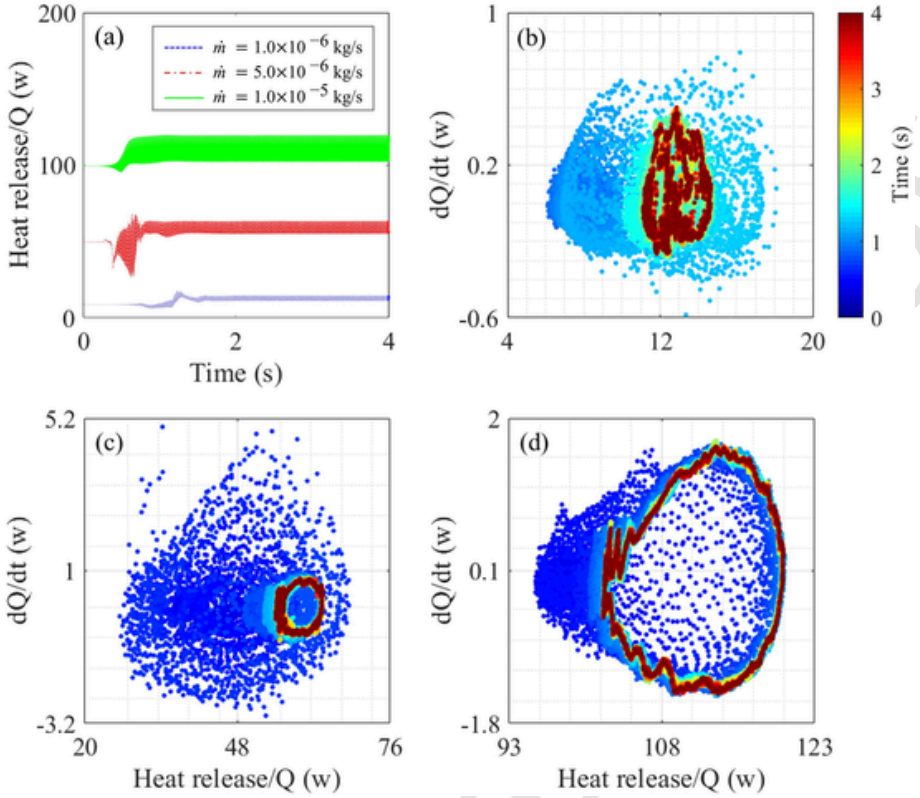

Fig. 9. (a) Time variation of the heat reaction Q_f and (b)-(d) the corresponding phase diagram, as w_{H_2}= 45\ %.and $\dot{m}$ is set to be 3 different values: i.e. (b) $\dot{m} = 1.0 \times 10^{-6} kg/s$, (c) $\dot{m} = 5.0 \times 10^{-6} kg/s$, (d) $\dot{m} = 1.0 \times 10^{-5} kg/s$.

responding time evolution of the phase diagrams of the acoustic pressure fluctuations.

The heat exchangers effect on combustion emissions of NO and NO_2 is also examined and compared, as shown in Fig. 10. Emission comparison is conducted before and after T_H of the heat exchangers is changed from 300 K to 1300 K at t = 2.0 s. In the axial direction, it can be seen from Fig. 10(b) and (f) that the variation tendency/profiles of chemical reactants and combustion products at T_H= 300 K and T_H= 1300 K are quite similar. Closer observation reveals that the NO emission is increased but NO_2 is decreased with the heat exchangers actuated. The generation rate of NO_2 is also decreased to a different level. One possible reason is that the limit cycle oscillations affect the NOx emission and the oxidation of NO is an exothermic reaction. As a result, the high temperature in downstream combustor has an inhibitory effect on those processes.

In the radial direction (see Fig. (d) and (h)), the consumption of both NH_3 and H_2 is improved while the radial profiles of χ_{O_2} (molar fraction) displays little discrepancy, before and after T_H is changed. This is most likely due to the fact that the fuel is mixed with a proportion of O_2 before injected at the inner inlet. Besides, with the acoustic pressure fluctuation, there is a periodic air flow squeezed from the bottom of the combustor. The mole fraction profiles of NO and NO_2 show similar changing trend in all cases which indicates the imperfect combustion of NH_3 is decreased.

There are two main contributions on the increase of NO emissions, when the mass flow rate increases at the same concentration. Firstly, by comparing the assumption of O_2 in two conditions, it is found that the molar fraction of unburned NH_3 and H_2 are smaller as well as the remaining O_2. This indicates that a more sufficient combustion occurs with a larger mass flow rate. In addition, the emission fraction of each product is determined by the reaction mechanism adopted. However, the chemical reaction can only be spontaneous beyond certain temperature. Some reactions involve both forward and backward generation processes between NO and NO_2. The contribution of each reaction equation must be considered in order to calculate the combustion products more accurately. However, this is not the focus of the current work. Since the temperature needed for the generation of NO_2 by burning NH_3 are higher than to NO, there are more unburned NH_3 diffusing to the region with relatively lower temperature with the increases of the inlet velocity, in which case NH_3 can only be oxidised to NO, instead of NO_2.

The correlation between the flame heat release and heat exchangers is analysed by comparing their time–frequency spectrum before and after the heat exchangers are actuated. This is shown in Fig. 13. It is obvious that the flame heat release and the heating flux from the heat exchangers are sharing similar frequency spectrum. The dominant mode and its harmonics are found to involved with frequency increase, as the heat exchangers are actuated.

The frequency spectrum of velocity fluctuation is further studied to investigate the nonlinearity of the system before and after the heat exchangers are actuated (t = 2.0 s), as shown in Fig. 14. As $\dot{m}$is set to three different values, both the dominant fluctuation amplitude and frequency are found to be increased, as the temperature of the heat exchanger is varied from 300 K to 1300 K (see Fig. 14(a, b and c)). Comparing Fig. 14(a) and (c) reveals that mode-switching occurs, as $\dot{m}$ is increased from $1.0 \times 10^{-6} kg/s$ to $1.0 \times 10^{-5} kg/s$ Comparing Fig. 14(a) and (c) shows that ω_1 is observed to shift from 178 Hz to 207.5 Hz by approximately 16.57%. Moreover, the frequency shift at ω_1 is also observed, as T_H is changed from 300 K to 1300 K. For example, ω_1 is observed to be shifted by 3.65% (from 178 Hz to 184.5 Hz) after the heat exchanger is actuated and $\dot{m} = 1.0 \times 10^{-6} kg/s$ This is probably because the increase of sound speed but the standing-wave mode-shape is unchanged.

UNCORRECTED PROOF

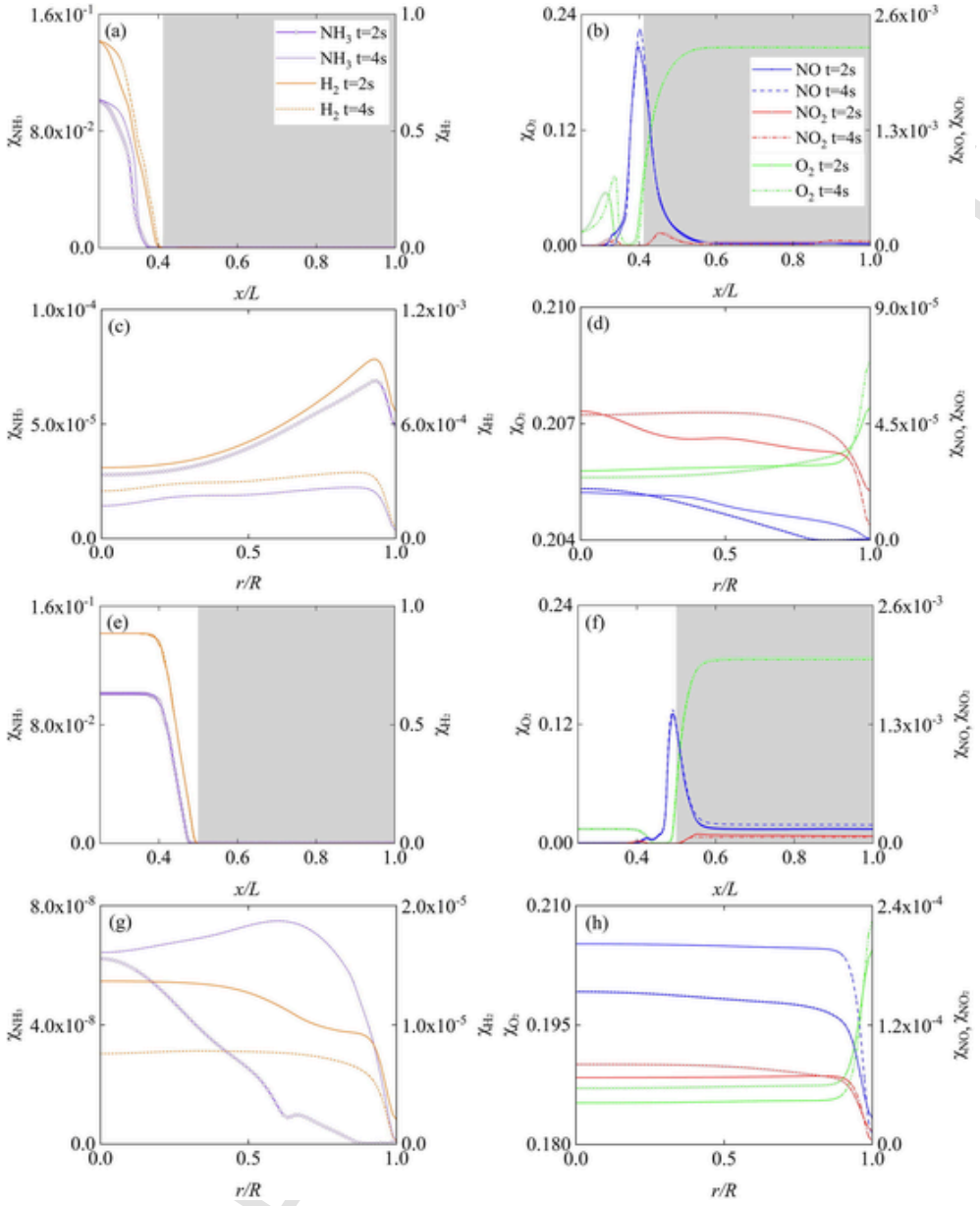

Fig. 10. The molar fraction of chemical reactants and product species varied in the axial (x/L) and radial (r/R) directions at pre-selected time steps. (a-d) $\dot{m} = 1.0 \times 10^{-6} kg/s$, (e-h) $\dot{m} = 1.0 \times 10^{-5} kg/s$ as $w_{H_2} = 45\%$; the temperature of the heat exchangers is set to 300 K at $t \leq 2.0$ and suddenly increase to 1300 K in a short period and remains constant at $2.0 < t \leq 4.0$ s

To shed lights on the damping mechanism of actuating the heat exchangers on combustion-driven oscillations, the phase angle between acoustic pressure and the flame heat release fluctuation at dominant frequencyω is determined and shown in Fig. 15. This is based on the well-known Rayleigh criteria [28,30,49]. It states that limit cycle oscillations may be produced when acoustic pressure and unsteady heat release are in phase. It can be seen from Fig. 15(a) that the amplitudes of both acoustic pressure and the heat of reaction are decreased, when the temperature of the heat exchanger are changed from 300 K to 1300 K. the phase difference between the heat of reaction and the acoustic pressure could be determined by working out the time delay between them. This is shown in Fig. 15(b) and Fig. 15(c).

At $t < 2.0$ s, the reaction heat release has a 67.5° phase advance compared to the acoustic pressure. However, at $t > 3.9$ s, the phase difference is changed to be −76.6°. This phase change/shift is the main reason why the combustion-driven oscillations [50,51] are attenuated somehow but smaller-amplitude limit cycles are still present, even with the heat exchangers temperature increased. The phase difference change is due to the change of the heat exchangers from absorbing heat to releasing heat to the surrounding flow. Further studies are conducted on determining the phase difference between the heat flux from the heat exchangers and the acoustic pressure, as shown in Fig. 15(d). It can be seen that the phase difference is approximately 145°. It means the acoustic pressure and unsteady heat release from the heat exchangers are out of phase. This explains why the limit cycles [52] are attenuated. This finding is consistent with Rayleigh criterion [53].

5. Discussion and conclusions

The hydrogen-ammonia-fueled flame producing pulsating oscillations and its impact on the thermodynamic properties in a standing-wave combustor with the heat exchangers confined are numerically investigated. More physical insights are obtained on the flame-flow-

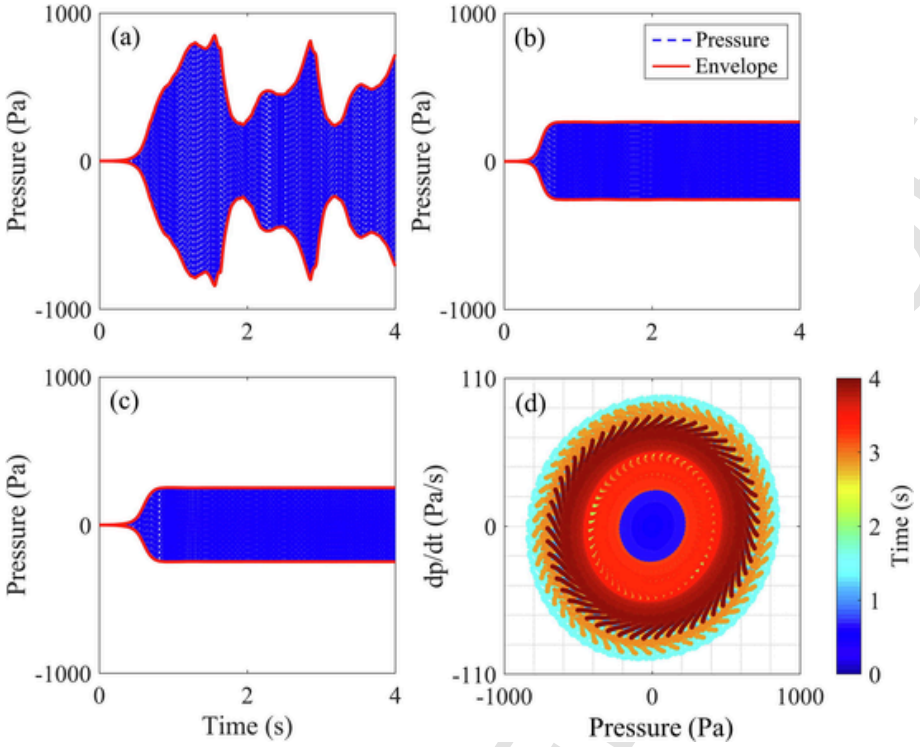

Fig. 11. Time evolution of the acoustic pressure, as $\dot{m} = 1.0 \times 10^{-5} kg/s$, and ṁ is set to the mass fraction of H_2 is set to be (a) $w_{H_2} = 15\backslash\ \%$, (b) $w_{H_2} = 45\backslash\ \%$, and (c) $w_{H_2} = 88.4\backslash\ \%$; (d) the corresponding phase diagram, as $\dot{m} = 1.0 \times 10^{-5} kg/s$ and $w_{H_2} = 15\backslash\ \%$.

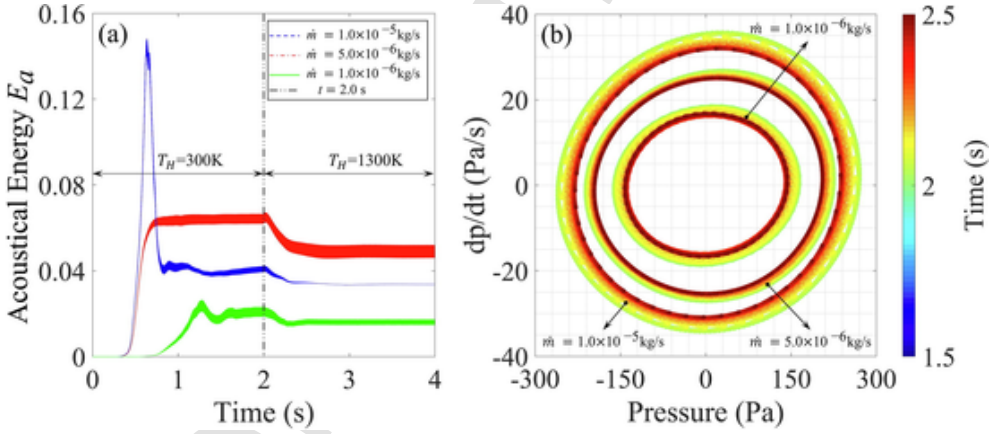

Fig. 12. (a) acoustical energy with time, as ṁ is set to three different value, and T_H of the heat exchangers is set to 300 K at $t \leq 2.0$ and slowly increase to 1300 K over 0.25 s and then remains constant at $2.25 \leq t \leq 4.0$ s; (b) Phase diagrams of acoustic pressure fluctuation with time under various ṁ.

acoustics dynamic interactions. It is found that the mass flow rate ṁ of NH_3 and H_2 mixture determines not only the pulsating combustion characteristics but also the molar fraction profiles of the combustion species. A larger percentage of NO is observed to be oxidized to NO_2 in the after-reaction zone along axial direction with the decrease of ṁ . Moreover, the conversion rate of NO_2 is also increased in radial direction when ṁ decreases. It is found that the temperature change of the heat exchanger also affects the distribution of reaction products. The conversion rate of NO_2 is declined on a different level after the heat exchanger is turned on. The reason why the heat exchangers are applicable to mitigate pulsating combustion-sustained oscillations is explained physically which is consistent with the Rayleigh criterion. Mode shift occurs as ṁ is increased. Additionally, the change of ṁ and the temperature of the heat exchangers can both lead to frequency shift. A quasi-periodic intermittent oscillation is observed when mass fraction of H_2 decreases to 15% and the combustion instability will be intensified with decreased $\dot{m}$ and wH_2 Furthermore, the combustion system nonlinearity sources are identified to be 1) the acoustic velocity, 2) flame released rate Q_f and 3) the heat exchanger Q_H. The present work sheds light on the physical mechanisms behind H_2-NH_3-burnt combustion instability. It also provided an alternative way of replacing hydrocarbon fuel to help reduce the greenhouse gas of CO_2 emission.

Acknowledgement

This work was financially supported by the University of Canterbury, New Zealand with Grant No. 452STUPDZ, and National Research Foundation, Prime Minister's Office, Singapore, with Grant No. NRF2016NRF-NSFC001-102 and National Natural Science Foundation of China (11661141020).

Appendix A:. Chemical reaction mechanism

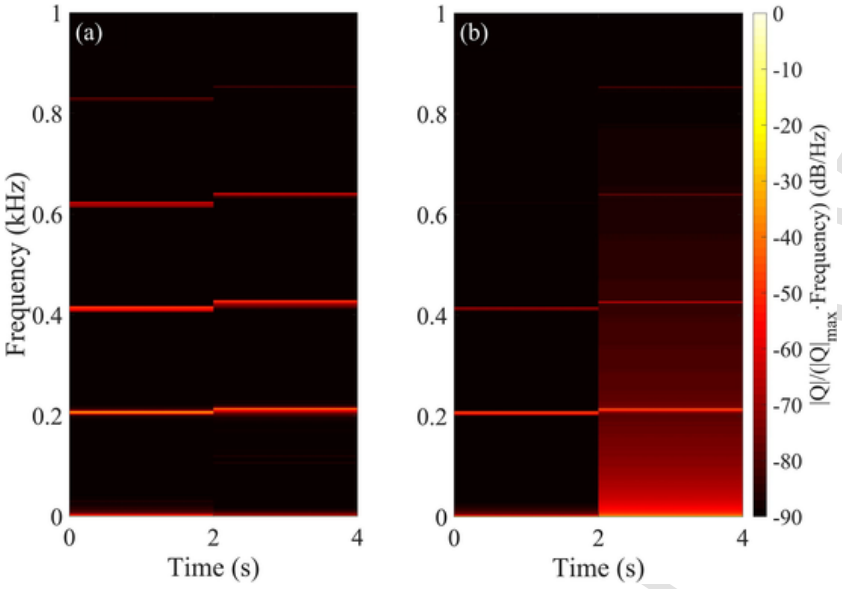

Fig. 13. Frequency spectrum and normalised signal energy of (a) heat of reaction and (b) the heat flux of the heat exchangers, as $\dot{m} = 1.0 \times 10^{-5} kg/s$, $w_{H_2} = 45\ \%$ and the temperature of the heat exchangers is set to 300 K at t ≤ 2.0 s and suddenly increase to 1300 K in a short period and remains constant at 2.0 < t ≤ 4.0 s.

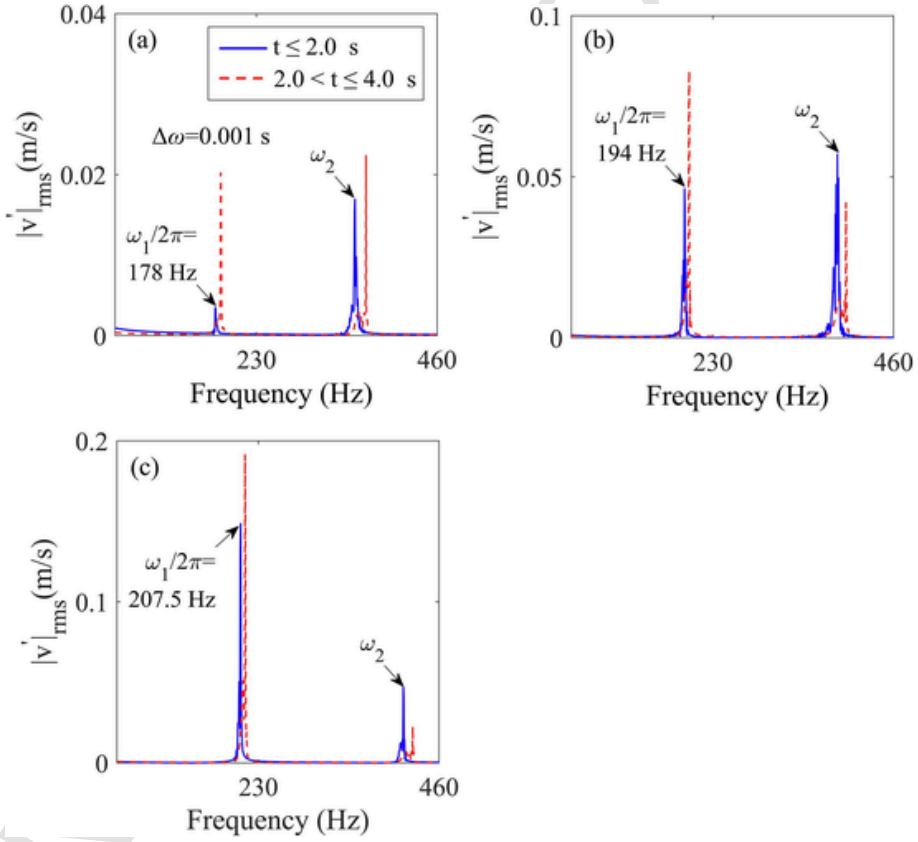

Fig. 14. The frequency spectrum of velocity fluctuation as $w_{H_2} = 45\ \%$, and ṁ is set to (a)$\dot{m} = 1.0 \times 10^{-6} kg/s$, (b) $\dot{m} = 5.0 \times 10^{-6} kg/s$, (c) $\dot{m} = 1.0 \times 10^{-5} kg/s$; T_H of the heat exchangers is set to be 300 K at t ≤ 2.0 s and suddenly increase to 1300 K in a short period and remains constant at 2.0 < t ≤ 4.0 s.

Appendix B:. Experimental setup

As shown in Fig. 4(c), an open-open Rijke tube with a total length of 1.0 m is designed and tested. A laminar premixed flame is anchored to a metal wire gauze placing on top of the Bunsen burner, i.e. $z = z_f$. And the axial position of the bottom open end is denoted by $z = 0$, and the gauze is at $z = z_2 \approx z_f$. The axial position of the flame can be varied from 4 percent to 35 percent with respect to the Rijke tube total length. The total length can be varied from 0.75 to 1.1 m. Propane is applied. Detailed information of the experimental rig can be found in Ref. [43].

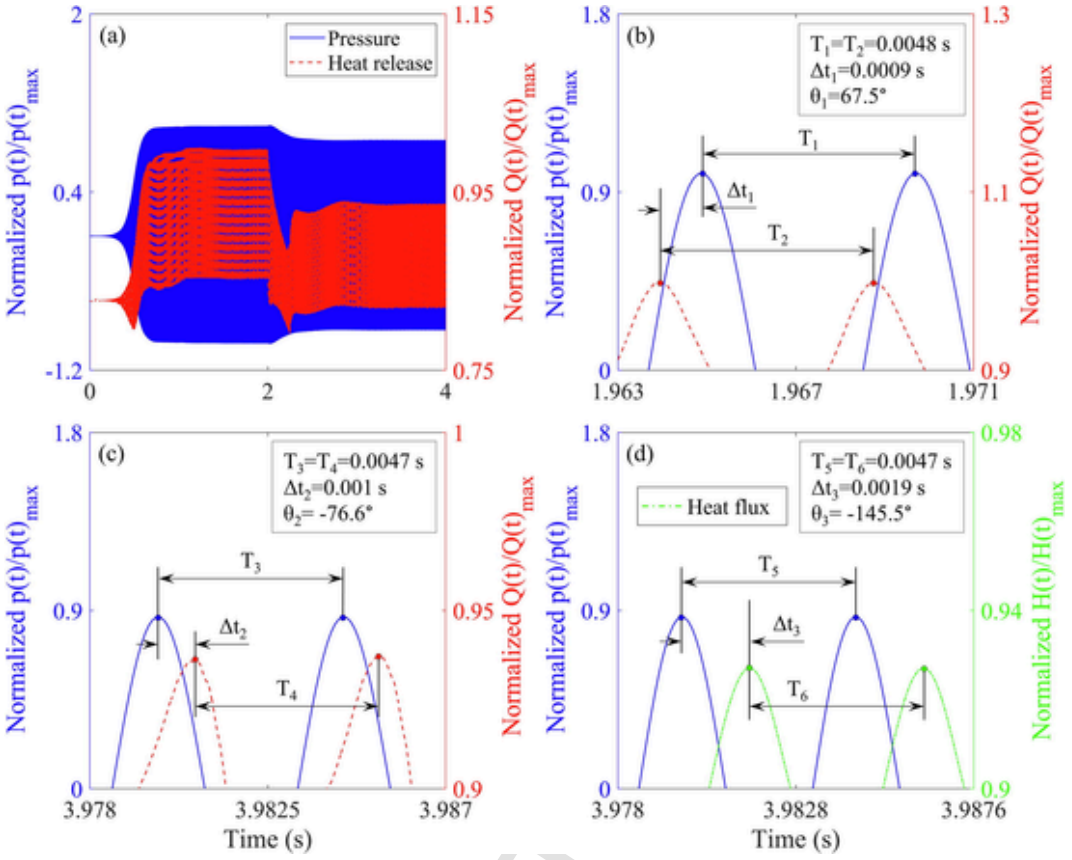

Fig. 15. Comparison of (a) pressure and heat release normalised by its maximum, (b) phase relationship between acoustic pressure and heat of reaction of the flame at $t < 2.0$ s and (c) phase relationship between acoustic pressure and heat of reaction of the flame at $t > 3.90$ s, (d) phase difference between the heat flux of the heat exchangers and the acoustic pressure. The phase angel can be calculated as $\theta = 360° \times \Delta t/T$, where ΔT is the duration of closest peaks between perturbations of pressure and heat release.

UNCORRECTED

Appendix Table 1
Skeletal model derived from the detailed model based in Okafor et al. H_2/NH_3 ignition, propagation and extinction.

	Reaction	A_k	β_k	E_k
1	$O + H_2 = H + OH$	3.87E + 04	2.7	6260
2	$O + HO_2 = OH + O_2$	2.00E + 13	0	0
3	$H + O_2 + M^{(a)} = HO_2 + M$	2.80E + 18	−0.86	0
4	$H + 2O_2 = HO_2 + O_2$	2.08E + 19	−1.24	0
5	$H + O_2 + H_2O = HO_2 + H_2O$	1.13E + 19	−0.76	0
6	$H + O_2 + N_2 = HO_2 + N_2$	2.60E + 19	−1.24	0
7	$H + O_2 = O + OH$	1.04E + 14	0	15,286
8	$H + OH + M^{(b)} = H_2O + M$	2.20E + 22	−2	0
9	$H + HO_2 = O_2 + H_2$	4.48E + 13	0	1068
10	$H + HO_2 = {}_2OH$	8.40E + 13	0	635
11	$OH + H_2 = H + H_2O$	2.16E + 08	1.51	3430
12	$2OH(+M^{(c)}) = H_2O_2(+M)$	7.40E + 13	−0.37	0
	Low pressure limit	2.30E + 18	−0.9	−1700
	Troe centering: a = 0.7346, T*** = 94, T* = 1756, T** = 5182			
13	$2OH = O + H_2O$	3.57E + 04	2.4	−2110
14	$OH + HO_2 = H_2O + O_2$	7.00E + 12	0	−1092.96
15	$OH + HO_2 = H_2O + O_2$	4.50E + 14	0	10929.6
16	$OH + H_2O_2 = HO_2 + H_2O$	1.70E + 18	0	29,410
17	$2HO_2 = O_2 + H_2O_2$	1.30E + 11	0	−1630
18	$2HO_2 = O_2 + H_2O_2$	4.20E + 14	0	12,000
19	$N + NO = N_2 + O$	2.70E + 13	0	355
20	$N + O_2 = NO + O$	9.00E + 09	1	6500
21	$N + OH = NO + H$	3.36E + 13	0	385
22	$N_2O + O = N_2 + O_2$	1.40E + 12	0	10,810
23	$N_2O + H = N_2 + OH$	3.87E + 14	0	18,880
24	$N_2O + OH = N_2 + HO_2$	2.00E + 12	0	21,060
25	$N_2O(+M^{(c)}) = N_2 + O(+M)$	7.91E + 10	0	56,020
	Low pressure limit	6.37E + 14	0	56,640
26	$HO_2 + NO = NO_2 + OH$	2.11E + 12	0	−480
27	$NO + O + M^{(c)} = NO_2 + M$	1.06E + 20	−1.41	0
28	$NO_2 + O = NO + O_2$	3.90E + 12	0	−240
29	$NO_2 + H = NO + OH$	1.32E + 14	0	360
30	$NH + H = N + H_2$	3.00E + 13	0	0
31	$NH + O = NO + H$	9.20E + 13	0	0
32	$NH + OH = HNO + H$	2.00E + 13	0	0
33	$NH + OH = N + H_2O$	5.00E + 11	0.5	2000
34	$NH + O_2 = HNO + O$	4.60E + 05	2	6500
35	$NH + O_2 = NO + OH$	1.30E + 06	1.5	100
36	$NH + NO = N_2O + H$	1.80E + 14	−0.351	−244
37	$NH + NO = N_2 + OH$	2.20E + 13	−0.23	0
38	$NH_2 + H = NH + H_2$	7.20E + 05	2.32	799
39	$NH_2 + O = HNO + H$	6.60E + 13	0	0
40	$NH_2 + OH = NH + H_2O$	4.00E + 06	2	1000
41	$NH_2 + HO_2 = NH_3 + O_2$	9.20E + 05	1.94	−1152
42	$2NH_2 = NH_3 + NH$	5.00E + 13	0	10,000
43	$NH_2 + NH = N_2H_2 + H$	5.00E + 13	0	0
44	$NH_2 + N = N_2 + 2H$	7.00E + 13	0	0
45	$NH_2 + NO = N_2 + H_2O$	2.80E + 20	−2.654	1258
46	$NH_2 + NO = NNH + OH$	2.30E + 10	0.425	−814
47	$NH_2 + NO_2 = N_2O + H_2O$	1.60E + 16	−1.44	268
48	$NNH = N_2 + H$	6.50E + 07	0	0
49	$NNH + O = N_2O + H$	1.00E + 14	0	0
50	$NNH + O = NH + NO$	5.00E + 13	0	0
51	$NNH + O_2 = N_2 + HO_2$	2.00E + 14	0	0
52	$NNH + O_2 = N_2 + H + O_2$	5.00E + 13	0	0
53	$H + NO + M^{(c)} = HNO + M$	4.48E + 19	−1.32	740
54	$HNO + H = H_2 + NO$	9.00E + 11	0.72	660
55	$HNO + OH = NO + H_2O$	1.30E + 07	1.9	−950
56	$HNO + O_2 = HO_2 + NO$	1.00E + 13	0	13,000
57	$NH_3 + H = NH_2 + H_2$	5.40E + 05	2.4	9915
58	$NH_3 + M = NH_2 + H + M$	6.60E + 17	0	97,300
59	$NH_3 + OH = NH_2 + H_2O$	2.00E + 06	2.04	566
60	$NH_3 + O = NH_2 + OH$	9.40E + 06	1.94	6460
61	$N_2H_2 + H = NNH + H_2$	8.50E + 04	2.63	230
62	$N_2H_2 + O = NNH + OH$	3.30E + 08	1.5	497
63	$N_2H_2 + OH = NNH + H_2O$	5.90E + 01	3.4	1360

where A_k ($m3/(kmol\hat{A}\cdot s)$) is pre-exponential factor of reaction rate; β_k is temperature exponent and E_k(J/kmol) is the activation energy of the reaction. (a) Enhancement factors: $O_2 = 0$, $H_2O = 0$, $N_2 = 0$; (b) Enhancement factors: $H_2 = 0.73$, $H_2O = 3.65$; (c) Enhancement factors: $H_2 = 2$, $H_2O = 6$.

References

[1] S Verhelst, Recent progress in the use of hydrogen as a fuel for internal combustion engines, Int. J. Hydrogen Energy 39 (2) (2014) 1071–1085.
[2] S Verhelst, T Wallner, Hydrogen-fueled internal combustion engines, Prog. Energy Combust. Sci. 35 (6) (2009) 490–527.
[3] A Bentaib, N Meynet, A Bleyer, Overview on hydrogen risk research and development activities: methodology and open issues, Nucl. Eng. Technol. 47 (1) (2015) 26–32.
[4] J Chen, An Empirical Study on China's Energy Supply-and-Demand Model Considering Carbon Emission Peak Constraints in 2030, Engineering 3 (4) (2017) 512–517.
[5] R. Service. Ammonia—A Renewable Fuel Made from Sun, Air, and Water—Could Power the Globe without Carbon. Science 2018: aau7489.
[6] F.J. Verkamp, M.C. Hardin, J.R. Williams. Ammonia combustion properties and performance in gas-turbine burners. In Symposium (International) on Combustion 1967 Jan 1 (Vol. 11, No. 1, pp. 985-992). Elsevier.
[7] C S Mørch, A Bjerre, M P Gøttrup, S C Sorenson, J Schramm, Ammonia/hydrogen mixtures in an SI-engine: Engine performance and analysis of a proposed fuel system, Fuel 90 (2) (2011) 854–864.
[8] A J Reiter, S C Kong, Combustion and emissions characteristics of compression-ignition engine using dual ammonia-diesel fuel, Fuel 90 (1) (2011) 87–97.
[9] C Zamfirescu, I Dincer, Using ammonia as a sustainable fuel, J. Power Sources 185 (1) (2008) 459–465.
[10] A J Reiter, S C Kong, Demonstration of compression-ignition engine combustion using ammonia in reducing greenhouse gas emissions, Energy Fuels 22 (5) (2008) 2963–2971.
[11] S Frigo, R Gentili, Analysis of the behaviour of a 4-stroke Si engine fuelled with ammonia and hydrogen, Int. J. Hydrogen Energy 38 (3) (2013) 1607–1615.
[12] J R Howell, M J Hall, J L Ellzey, Combustion of hydrocarbon fuels within porous inert media, Prog. Energy Combust. Sci. 22 (2) (1996) 121–145.
[13] J H Lee, S I Lee, O C Kwon, Effects of ammonia substitution on hydrogen/air flame propagation and emissions, Int. J. Hydrogen Energy 35 (20) (2010) 11332–11341.
[14] J Li, H Huang, N Kobayashi, Z He, Y Nagai, Study on using hydrogen and ammonia as fuels: Combustion characteristics and NOx formation, Int. J. Energy Res. 38 (9) (2014) 1214–1223.
[15] S I Lee, D H Um, O C Kwon, Performance of a microthermophotovoltaic power system using an ammoniahydrogen blend-fueled micro-emitter, Int. J. Hydrogen Energy 38 (22) (2013) 9330–9342.
[16] D H Um, J M Joo, S Lee, O C Kwon, Combustion stability limits and NOx emissions of nonpremixed ammonia-substituted hydrogen–air flames, Int. J. Hydrogen Energy 38 (34) (2013) 14854–14865.
[17] A Valera-Medina, M Gutesa, H Xiao, D Pugh, A Giles, B Goktepe, R Marsh, P Bowen, Premixed ammonia/hydrogen swirl combustion under rich fuel conditions for gas turbines operation, Int. J. Hydrogen Energy 44 (16) (2019) 8615–8626.
[18] C Lhuillier, P Brequigny, F Contino, C Mounaïm-Rousselle, Experimental study on ammonia/hydrogen/air combustion in spark ignition engine conditions, Fuel 269 (2020) 117448.
[19] C Duynslaegher, H Jeanmart, J Vandooren, Ammonia combustion at elevated pressure and temperature conditions, Fuel 89 (11) (2010) 3540–3545.
[20] C Duynslaegher, F Contino, J Vandooren, H Jeanmart, Modeling of ammonia combustion at low pressure, Combust. Flame 159 (9) (2012) 2799–2805.
[21] J Li, H Huang, L Deng, Z He, Y Osaka, N Kobayashi, Effect of hydrogen addition on combustion and heat release characteristics of ammonia flame, Energy 175 (2019) 604–617.
[22] J Otomo, M Koshi, T Mitsumori, H Iwasaki, K Yamada, Chemical kinetic modeling of ammonia oxidation with improved reaction mechanism for ammonia/air and ammonia/hydrogen/air combustion, Int. J. Hydrogen Energy 43 (5) (2018) 3004–3014.

UNCORRECTED PROOF

[23] N A Hussein, A Valera-Medina, A S Alsaegh, Ammonia-hydrogen combustion in a swirl burner with reduction of NOx emissions, Energy Procedia 158 (2019) 2305–2310.
[24] J O'Connor, V Acharya, T Lieuwen, Transverse combustion instabilities: Acoustic, fluid mechanic, and flame processes, Prog. Energy Combust. Sci. 49 (2015) 1–39.
[25] Y Huang, V Yang, Dynamics and stability of lean-premixed swirl-stabilized combustion, Prog. Energy Combust. Sci. 35 (4) (2009) 293–364.
[26] Y Yu, J C Sisco, S Rosen, A Madhav, W E Anderson, Spontaneous longitudinal combustion instability in a continuously-variable resonance combustor, J. Propul. Power 28 (5) (2012) 876–887.
[27] J G Lee, D A Santavicca, Experimental diagnostics for the study of combustion instabilities in lean premixed combustors, J. Propul. Power 19 (5) (2003) 735–750.
[28] L Rayleigh, The explanation of certain acoustical phenomena, Nature 18 (1878) 319–321.
[29] Q. Song, A. Fang, G. Xu, Y. Xu, W. Huang. Experimental investigation of thermoacoustic oscillations in syngas premixed multi-swirler model combustors. In ASME Turbo Expo 2009: Power for Land, Sea, and Air 2009 Jan 1 (pp. 669-678). American Society of Mechanical Engineers Digital Collection.
[30] S L Bragg, Noise and oscillations in jet engines, Nature 201 (1964) 123–129.
[31] G Wang, Y Li, L Li, F Qi, Experimental and theoretical investigation on cellular instability of methanol/air flames, Fuel 225 (2018) 95–103.
[32] K Lee, H Kim, P Park, S Yang, Y Ko, CO_2 radiation heat loss effects on NOx emissions and combustion instabilities in lean premixed flames, Fuel 106 (2013) 682–689.
[33] J Li, Y Xia, A S Morgans, X Han, Numerical prediction of combustion instability limit cycle oscillations for a combustor with a long flame, Combust. Flame 185 (2017) 28–43.
[34] B F Cintra, E C Fernandes, Thermoacoustic instabilities of lean disc flames, Fuel 184 (2016) 973–986.
[35] J M Pires, E C Fernandes, Combined effect of equivalence ratio and velocity gradients on flame stability and emission formation, Fuel 222 (2018) 800–809.
[36] B T Chu, L S Kovásznay, Non-linear interactions in a viscous heat-conducting compressible gas, J. Fluid Mech. 3 (5) (1958) 494–514.
[37] W.M. Pitts. Assessment of theories for the behaviour and blowout of lifted turbulent jet diffusion flames. In Symposium (international) on combustion 1989 Jan 1 (Vol. 22, No. 1, pp. 809-816). Elsevier.
[38] Y C Chao, Y L Chang, C Y Wu, T S Cheng, An experimental investigation of the blowout process of a jet flame, Proc. Combust. Inst. 28 (1) (2000) 335–342.
[39] Y C Chao, C Y Wu, K Y Lee, Y H Li, R H Chen, T S Cheng, Effects of dilution on blowout limits of turbulent jet flames, Combust. Sci. Technol. 176 (10) (2004) 1735–1753.
[40] V.R. Hasti, P. Kundu, G. Kumar, S.A. Drennan, S. Som, J.P. Gore. A Numerical Study of Flame Characteristics during Lean Blow-Out in a Gas Turbine Combustor. In 2018 Joint Propulsion Conference 2018 (p. 4955).
[41] M A Heckl, Non-linear acoustic effects in the Rijke tube, Acta Acust. Acust. 72 (1) (1990) 63–71.
[42] D Zhao, Transient growth of flow disturbances in triggering a Rijke tube combustion instability, Combust. Flame 159 (6) (2012) 2126–2137.
[43] D Zhao, Z H Chow, Thermoacoustic instability of a laminar premixed flame in Rijke tube with a hydrodynamic region, J. Sound Vib. 332 (2013) 3419–3437.
[44] A P Dowling, Nonlinear self-excited oscillations of a ducted flame, J. Fluid Mech. 346 (1997) 271–290.
[45] S Hemchandra, Premixed flame response to equivalence ratio fluctuations: Comparison between reduced order modeling and detailed computations, Combust. Flame 159 (12) (2012) 3530–3543.
[46] K Kashinath, S Hemchandra, M P Juniper, Nonlinear phenomena in thermoacoustic systems with premixed flames, J. Eng. Gas Turb. Power 135 (6) (2013) 061502.
[47] K Kashinath, S Hemchandra, M P Juniper, Nonlinear thermoacoustics of ducted premixed flames: the influence of perturbation convection speed, Combust. Flame 160 (12) (2013) 2856–2865.
[48] O. Ditlevsen, H.O. Madsen, 1996. Structural Reliability Methods. John Wiley & Sons, Baffins Lane, England.
[49] S A Pawar, R Vishnu, M Vadivukkarasan, M V Panchagnula, R I Sujith, Intermittency route to combustion instability in a laboratory spray combustor, J. Eng. Gas Turbines Power 138 (4) (2016) 041505.
[50] J Zhang, A Ratner, Experimental study on the excitation of thermoacoustic instability of hydrogen-methane/air premixed flames under atmospheric and elevated pressure conditions, Int. J. Hydrogen Energy 44 (39) (2019) 21324–21335.
[51] N A Baraiya, S R Chakravarthy, Excitation of high frequency thermoacoustic oscillations by syngas in a non-premixed bluff body combustor, Int. J. Hydrogen Energy 44 (29) (2019) 15598–15609.
[52] Y J Kim, Y Yoon, M C Lee, On the observation of high-order, multi-mode thermoacoustic combustion instability in a model gas turbine combustor firing hydrogen containing syngases, Int. J. Hydrogen Energy 44 (21) (2019) 1111–11120.
[53] Q Chen, B Wang, H Zhang, Y Zhang, W Gao, Numerical investigation of H2/air combustion instability driven by large scale vortex in supersonic mixing layers, Int. J. Hydrogen Energy 41 (4) (2016) 3171–3184.

UNCORRECTED PROOF